Ambient Pressure Sensitivity of Subharmonic Vibrating Single Microbubbles

Spiekhout, Sander; Wang, Yuchen; Segers, Tim; Kooiman, Klazina; Versluis, Michel; Voorneveld, Jason; de Jong, Nico; Bosch, Johannes G.

DOI
10.1016/j.ultrasmedbio.2025.01.016

Publication date
2025

Document Version
Final published version

Published in
Ultrasound in Medicine and Biology

Citation (APA)
Spiekhout, S., Wang, Y., Segers, T., Kooiman, K., Versluis, M., Voorneveld, J., de Jong, N., & Bosch, J. G. (2025). Ambient Pressure Sensitivity of Subharmonic Vibrating Single Microbubbles. *Ultrasound in Medicine and Biology*, *51*(6), 931-940. https://doi.org/10.1016/j.ultrasmedbio.2025.01.016

Ultrasound in Medicine & Biology 51 (2025) 931−940

Contents lists available at ScienceDirect

Ultrasound in Medicine & Biology

journal homepage: www.elsevier.com/locate/ultrasmedbio

Original Contribution

Ambient Pressure Sensitivity of Subharmonic Vibrating Single Microbubbles

Sander Spiekhout [a,*], Yuchen Wang [a], Tim Segers [b], Klazina Kooiman [a], Michel Versluis [c], Jason Voorneveld [a], Nico de Jong [a,d], Johannes G. Bosch [a]

[a] Biomedical Engineering, Department of Cardiology, Cardiovascular Institute, Erasmus Medical Center, Rotterdam, The Netherlands
[b] BIOS/Lab on a Chip Group, University of Twente, Enschede, The Netherlands
[c] Physics of Fluids Group, TechMed Center, University of Twente, Enschede, The Netherlands
[d] Department of Imaging Physics, Delft University of Technology, Delft, The Netherlands

ARTICLE INFO

Keywords:
Lipid-coated microbubbles
Ultrasound contrast agents
Blood pressure estimation
Ambient pressure sensitivity
Subharmonic-aided pressure estimation

ABSTRACT

Objective: The response of ultrasound contrast agents is sensitive to ambient pressure, especially *via* their scattered subharmonic signal, which makes them a promising candidate for non-invasive pressure measurements *in vivo*. This work aimed to understand the sensitivity to ambient pressure of subharmonic oscillations from single microbubbles.

Methods: The subharmonic oscillation amplitude of single microbubbles in response to varying ambient pressure was studied both experimentally and numerically. In experiment, approximately 2200 single microbubbles from a monodisperse population were measured at a driving frequency close to twice their resonance frequency.

Results: The results of the numerical simulations and experiments show that a pressure change leads to a small size change in the bubble that then changes the lipid packing density, and with that the stiffness of the bubble shell.

Conclusion: The dependency of subharmonic oscillation amplitude to changes in ambient pressure can be explained by a shift in the resonance frequency of the bubble as a function of ambient pressure. The subharmonic response increases with ambient pressure when the resonance frequency shifts toward half the driving frequency and decreases when the resonance frequency shifts away from half the driving frequency. These findings help to understand non-invasive pressure sensing through subharmonic ultrasound imaging.

Introduction

From the early days of ultrasound contrast agents, it has been known that the acoustic behavior of microbubbles depends on the ambient pressure, *i.e.*, the semi-static surrounding pressure a bubble is experiencing. Therefore, microbubbles can, in principle, be used to measure changes in ambient pressure, *e.g.*, for the non-invasive measurement of blood pressure. Blood pressure measurement using contrast-enhanced ultrasound was first suggested by Tickner [1], where the resonance frequency of a bubble was directly related to its size at the corresponding ambient pressure. A different idea was proposed by Bouakaz et al. [2], who aimed to fracture bubbles with a rigid coating and subsequently envisioned using the dissolution rate of the released free gas bubble to measure the ambient pressure. Another idea, which did not specifically require bubble destruction, was proposed by Shi et al. [3], who reasoned that the subharmonic scattering amplitude, *i.e.*, at a harmonic below the driving frequency, could be used to estimate ambient pressure.

Recently, subharmonic sensitivity to ambient pressure has garnered more attention through the Subharmonic Aided Pressure Estimation (SHAPE) technique [4−6], which is also the subject of a clinical trial (NCT05470205). Studies employing SHAPE have identified an occurrence, growth and saturation stage for subharmonic scattering as a function of ambient pressure and used the linear growth stage to semi-qualitatively measure blood pressure. However, the mechanisms underlying SHAPE are not fully understood. There is little consensus on the dependency of the subharmonic signal to ambient pressure, *i.e.*, the change (and direction of change) in subharmonic scattered signal as a function of ambient pressure, even for well-controlled *in vitro* studies using the same contrast agents [7]. Subharmonic scattering can decrease or increase with ambient pressure increases, and this sensitivity is found to also depend on acoustic pressure amplitude, frequency, as well as on the initial ambient pressure [5,8].

Free gas bubbles start oscillating at subharmonic frequencies when they are driven at sufficiently large vibrational amplitudes [9] irrespective of the driving frequency [10,11]. These higher oscillation-amplitude subharmonics are often employed as an indicator for the onset of inertial cavitation [12]. A numerical investigation by Katiyar et al. [13] into the ambient pressure sensitivity of free gas bubble subharmonics (and simple encapsulated microbubbles) under high driving pressures identified

* Corresponding author. Biomedical Engineering, Thorax Center, Erasmus Medical Center, EE-2302, Wytemaweg 80, Rotterdam, 3015 CN, The Netherlands.
E-mail address: sanderspiekhout@gmail.com (S. Spiekhout).

https://doi.org/10.1016/j.ultrasmedbio.2025.01.016
Received 4 April 2024; Revised 22 January 2025; Accepted 24 January 2025

a resonance effect explaining the subharmonic response to ambient pressure. A critical ratio of approximately 1.6 between driving frequency and microbubble resonance frequency at ambient pressure was found, for which the subharmonics reached a maximum. Below this ratio (1.4 −1.6), subharmonic amplitude generally increased with additional ambient pressure due to the corresponding rise in natural frequency. Conversely, for ratios above 2.1, subharmonics were found to decrease [13]. However, their model (based on the BUBBLESIM simulation code [14]) did not account for shell buckling and rupture, leaving the ambient pressure sensitivity of subharmonics at low acoustic pressure for lipid-coated agents, such as SonoVue, unexplained [15].

Lipid-coated microbubbles experience a sudden change in shell elasticity upon buckling, resulting in a much lower vibrational amplitude threshold for subharmonic generation [9,16]. The abrupt change in shell elasticity introduces a stronger and more complex relationship between resonance frequency and ambient pressure [17,18]. The generation of subharmonics at lower vibrational amplitudes is of interest due to the reduced risk of acoustic deflation [19], offering greater potential for repeatable subharmonic versus ambient pressure behavior. Studies employing low acoustic-amplitude subharmonics often report increasing subharmonics with rising hydrostatic pressure, which is attributed to microbubbles that are close to buckling (*i.e.*, those with low initial surface tension) [20,21]. However, other studies have shown that subharmonic scattering at a fixed acoustic pressure amplitude can increase or decrease by adjusting the ultrasound driving frequency [22], suggesting resonance frequency dependence similar to that observed for high oscillation amplitude-driven subharmonics [13]. Typical *in vitro* subharmonic pressure sensitivity studies employ pulse-echo to measure (bulk) subharmonic scattering of an ensemble of microbubble sizes, which provides limited information on single bubble dynamics. Faez et al. [15] managed to measure subharmonic scattering while applying a dynamic ambient pressure. This study showed that in a batch of polydisperse microbubbles, subharmonic scattering can indeed change with ambient pressure, and the preferential dependency of the subharmonic response on ambient pressure changes with driving frequency. However, deducing the exact mechanism responsible for this shift was difficult as bubble sizes were not known.

Here, we used a narrow size distribution of microbubbles that provided a starting point to model and understand the subharmonic oscillation behavior in response to pressure change. We utilized the acoustic camera approach of Renaud et al. [23], which then allowed acoustic characterization of freely oscillating, single microbubbles. We focused primarily on subharmonics at low-oscillation amplitudes, as these can be experimentally verified using the acoustic camera, but for completeness sake, subharmonics at higher oscillation amplitudes were treated separately numerically in Appendix C. In this study, we use the acoustic camera in conjunction with numerical simulations to unravel the mechanisms underlying the ambient pressure sensitivity of subharmonic microbubble vibrations.

Theory

The dynamics of a lipid-coated microbubble to an acoustic pulse are commonly modeled with the Marmottant model [17], which is based on a Rayleigh Plesset-type equation and accounts for the viscoelastic properties of a lipid-shelled microbubble, including buckling and rupture mechanics (eqn [1]):

$$\rho\left(\ddot{R}R+\frac{3}{2}\dot{R}^2\right)=\left(P_0+\frac{2\sigma(R_0)}{R_0}\right)\left(\frac{R_0}{R}\right)^{3\kappa}-\frac{4\mu_L\dot{R}}{R}-P_{amb}-P_a(t)-\frac{2\chi}{R}\left(\frac{R^2}{R_0}-1\right)-\frac{4\kappa_s\dot{R}}{R^2}. \tag{1}$$

Here, R is the instantaneous bubble radius with its time derivatives denoted by overdots, and the initial radius is R_0. P_a is the acoustic driving pressure and P_{amb} the ambient pressure. μ_L is the viscosity of the liquid surrounding the microbubble and the liquid density is ρ. κ is the polytropic exponent of the gas in the core.

The lipid shell protects the bubble against dissolution by lowering the initial surface tension $\sigma(R_0)$. Additionally, the viscoelastic shell adds a shell viscosity k_s and a surface elasticity χ, where χ is defined as the derivative of the size-dependent surface tension $\sigma(R)$ with respect to the microbubble surface area, A: $\chi = A\frac{d\sigma(R)}{dA}$. To account for the buckling and rupture mechanics of the shell, $\sigma(R)$ is a piecewise function of R given by eqn (2):

$$\sigma(R)=\begin{cases}0 & \text{if } R\le R_b\\ \chi\left(\frac{R^2}{R_b^2}-1\right) & \text{if } R_b\le R\le R_r\\ \sigma_w & \text{if } R_r\le R,\end{cases} \tag{2}$$

with σ_w the surface tension of water. Eqn (2) shows that the surface elasticity is only non-zero in the elastic regime bounded by the buckling radius R_b and rupture radius R_r. This elastic regime is limited to a few percent of the initial radius, depending on χ.

As a result of the buckling and rupture mechanics, the effective surface elasticity experienced by the system depends on the microbubble oscillation amplitude [24] as well as on minor size changes such as those imposed by static pressure changes [25,26]; *i.e.*, it depends on driving and ambient pressure, respectively. As microbubble oscillation amplitudes used in imaging typically extend beyond the elastic regime, it is useful to consider an effective stiffness, χ_{eff}, which is the χ averaged over (part of) the microbubble response (eqn [3]) [18]:

$$\chi_{eff}=\frac{1}{t_2-t_1}\int_{t_1}^{t_2}A\frac{d\sigma(R)}{dA}dt, \tag{3}$$

where t_1 and t_2 are arbitrary time points. A change in χ_{eff} results in a change in the effective resonance frequency $f_{0,eff}$ of the system. $f_{0,eff}$ follows from a linearization of eqn (1) [27]:

$$f_{0,eff}=\frac{1}{2\pi R_0}\sqrt{\frac{1}{\rho}\left(3\kappa P_{amb}+(3\kappa-1)\frac{2\sigma(R_0)}{R_0}+\frac{4\chi_{eff}}{R_0}\right)}. \tag{4}$$

Eqn (4) shows an explicit (P_{amb}) and implicit (R_0, $\sigma(R_0)$ and χ_{eff}) dependency on P_{amb}, with χ_{eff} potentially outweighing the other terms by two orders of magnitude [18].

The amplitude dependency of $f_{0,eff}$ has found widespread use in ultrasound imaging, for example through amplitude modulation [28]. While the P_{amb} dependency of $f_{0,eff}$ and its effect on fundamental scattering has previously been investigated [18], here we investigated the P_{amb} dependency of $f_{0,eff}$ and its effect on the subharmonic response, starting with numerical simulations.

Numerical methods

Simulated microbubble responses were generated by solving eqn (10), as described in [29]. The medium and shell parameters used in the simulations are listed in Table 1. The base $P_{amb,0}$ was set to 104 kPa to match the hydrostatic pressure experienced by the microbubbles in the experimental setup and liquid viscosity was doubled to account for thermal damping [30]. Non-physical transitions of surface elasticity at the buckling and rupture points were avoided by using the smoothing boundary function, as described in [31], with a smoothing value of 5000 N/m.

An ambient pressure, P_{amb}, was applied by a sinusoidal pressure pulse around the base P_{amb} with five cycles at 20 kHz (total duration 250 µs) with a pressure amplitude of 20 mm Hg (~2.7 kPa), similar to that of a cardiac cycle. The period of the pressure pulse allowed for single microbubbles to be characterized over a few ambient pressure cycles. The acoustic driving pulse was set to a pressure amplitude of 100 kPa,

Table 1
Physical properties used in numerical simulations

Property	Symbol	Value	Unit
Stiffness	χ	0.65	N/m
Shell viscosity	κ_s	1e-9	kg/s
Density	ρ	1000	kg/m^3
Ambient pressure	$P_{amb,0}$	104	kPa
Polytropic index	κ	1.07	[-]
Speed of sound	C	1483	m/s
Liquid viscosity	μ_L	$2\times$1e-3	Pa/s

without tapering, and lasted the entire 250 µs duration of the dynamic P_{amb}.

To study the effects of microbubble size and initial surface tension, $\sigma(R_0)$, on microbubble dynamics, subharmonic oscillation amplitude responses were simulated for radii R_0 from 1.6 to 2.3 m, which corresponded with the span of microbubble sizes used in the experiments, in 16 steps, and $\sigma(R_0)$ in 32 increments of 1 mN/m starting from 0 mN/m. The driving frequency f_T was set to either 4.0, 4.5 or 5.5 MHz (1000, 1125 or 1375 cycles, respectively) while keeping a constant acoustic pressure amplitude of 100 kPa. These f_T were selected as this was below (4.0 MHz), approximately (4.5 MHz) and above (5.5 MHz) twice the resonance frequency f_0 of the 2.0 µm microbubble of interest.

The subharmonic strain component *subH* was isolated from the simulated *R-t* curves, as described in Appendix A.

Numeric results

Figure 1 shows the result of the numerical simulations for a microbubble with a resting radius of 2.07 µm in response to a driving frequency of 4.5 MHz (approximately twice its resonance frequency). Figure 1a plots *subH* versus time for two initial surface tension values (2 mN/m, close to buckling, in blue; 19 mN/m, in the elastic regime, in orange) and the dotted line indicates the ambient pressure cycle. Figure 1b then displays *subH* as a function of the ambient pressure. It shows a nearly linear trend of the subharmonic response with P_{amb}, with a positive and negative slope for the two initial surface tensions. The subharmonic strain amplitude ($subH(P_{amb})$) was fitted with respect to P_{amb} using a first-order polynomial function to quantify the subharmonic behavior (eqn [5]):

$$subH(P_{amb}) = S_{subH}\cdot P_{amb} + a_{subH}. \tag{5}$$

Here S_{subH} is the slope of *subH* with respect to P_{amb}, which we will term the subharmonic sensitivity to ambient pressure, and the constant term a_{subH} is the *subH* at $P_{amb,0} = 104$ kPa. To quantify the linearity and drift of S_{subH}, a coefficient of determination (R^2) was extracted from the fit. *subH* was extracted from these two microbubble responses and plotted as a function of time in Figure 1a and as a function of P_{amb} in Figure 1b over the duration of one P_{amb} cycle (50 s).

Note that for the nearly buckled microbubble ($\sigma(R_0) = 2$ mN/m), the response (blue) decreases with P_{amb} (black dashed line shows fit), whereas for the elastic microbubble ($\sigma(R_0) = 19$ mN/m), its response (orange) increases with ambient pressure. As we are interested in the relationship between $f_{0,eff}$ and subharmonic behavior, from the microbubble responses simulated using eqn (1), $f_{0,eff}$ was extracted by solving eqns (3) and (4) on a two-cycle basis ($t_2 = t_1 + 2/f_T$), thereby capturing the changes on the subharmonic timescale. The resulting $f_{0,eff}$ was divided by half the driving frequency $f_T/2$, *i.e.*, representative of the subharmonic frequency, and plotted in Figure 1c.

Figure 1c shows that the elastic microbubble has a higher $f_{0,eff}$ and therefore a higher χ_{eff} than the buckled microbubble because it effectively spends more time in the elastic regime. Figure 1c also shows that $f_{0,eff}$, and thus χ_{eff}, decreases with increasing P_{amb} for both microbubbles as they are pushed further into the (tensionless) buckled regime. Here the crucial difference between the two examples is that $f_{0,eff}$ thereby moves away from $f_T/2$ ($f_{0,eff} > f_T/2$; decreasing *subH*) for the buckled microbubble, and that it moves toward $f_T/2$ for the elastic microbubble (increasing subH).

Expanding the results to the full parameter study, S_{subH}, a_{subH} and R^2 are presented as false-color maps in Figure 2. The first column in Figure 2 (a, d, g) shows the S_{subH} values color-coded red for positive values and blue for negative values. The middle column in Figure 2 (b, e, h) shows the a_{subH} values and the right column in Figure 2 (c, f, i) shows the R^2 values. Increasing f_T results in a left shift of the characteristics in the color maps.

To further investigate the $f_{0,eff}$ dependency of the subharmonic behavior, the contour of $f_{0,eff} = f_T/2$ was extracted by solving eqns (3) and (4) over the entire 250 µs duration. The result is plotted with a black dashed line in all the figures. The $f_{0,eff} = f_T/2$ line corresponds well in location with the peak a_{subH}, *i.e.*, the strongest (baseline) subharmonic response, found there. Interestingly, the $f_{0,eff} = f_T/2$ line also delineates the regimes where negative or positive sensitivity is expected.

From Figure 2, it could also be observed that negative sensitivity generally corresponded with lower $\sigma(R_0)$ values, where the χ_{eff} was (already) lower. Second, we observed in the left column that the red region was narrower than the blue region, indicating that negative

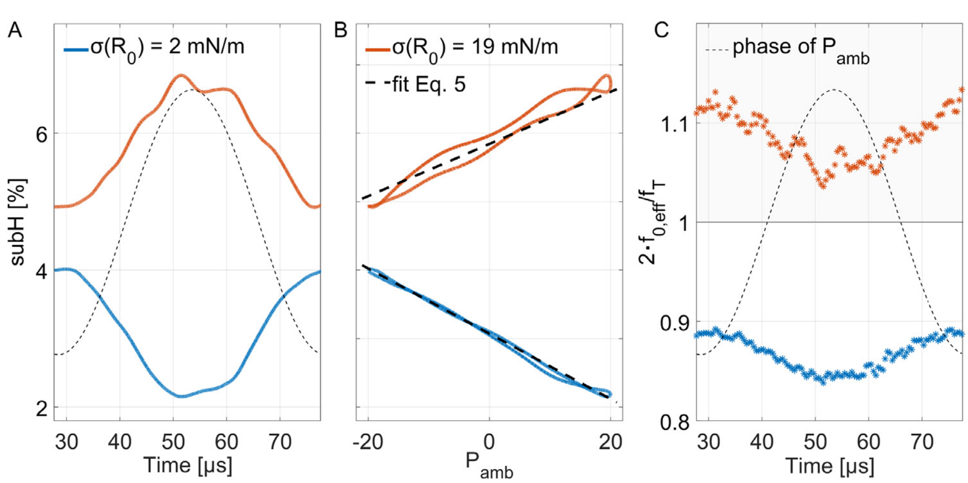

Figure 1. Subharmonic strain amplitude *subH* (a) as a function of time and (b) as a function of P_{amb}, which was used to fit eqn (5). (c) Extracted $f_{0,eff}$ from solving eqns (3, 4) on a two-cycle timescale. This shows that the nearly buckled microbubble's response decreased in *subH* with increasing P_{amb}, whereas the elastic microbubble's response increased. It also shows a higher resonance frequency for the elastic bubble and a decrease with increasing P_{amb} for both microbubbles.

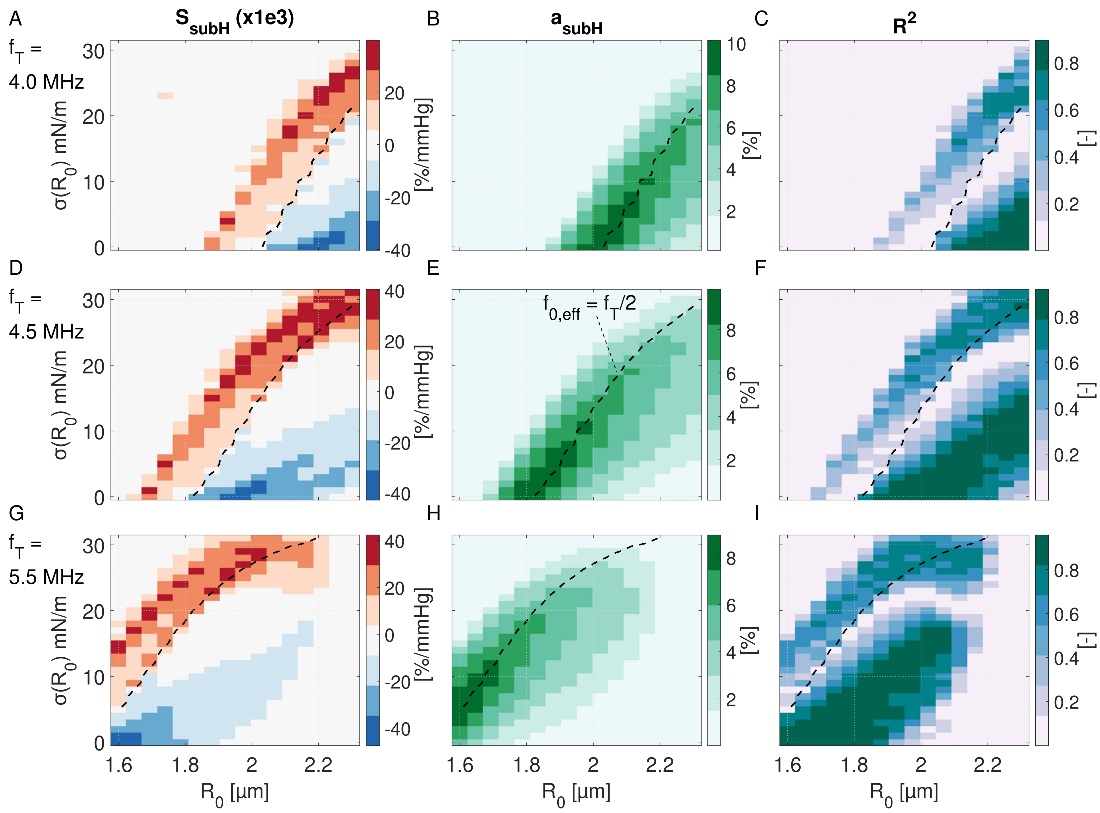

Figure 2. (a, d, g) Simulated subharmonic sensitivity to ambient pressure S_{subH}, (b, e, h) baseline subharmonic strain magnitude a_{subH} and (c, f, i) R^2 values of the fit to eqn (5) as a function of R_0 and $\sigma(R_0)$. The top row was simulated with a f_T of 4.0 MHz, middle row with 4.5 MHz and bottom row with 5.5 MHz.

sensitivity was more likely to occur. Experiments designed to confirm the driving frequency dependence of the subharmonic ambient pressure sensitive response are described in the next section.

Experimental methods

Microbubbles were formed by flow focusing using perfluorobutane (C_4F_{10}) as the gas and an aqueous lipid mixture consisting of DSPC: DPPE-PEG5000:Pluronic F68 in a 81:9:10 molar ratio within a microfluidic chip [32]. The resulting microbubbles were collected in a gas-tight medical vial prefilled with C_4F_{10} and stored for 1 d. Size was measured using a Coulter Counter (Multisizer 3, Beckman Coulter, Mijdrecht, The Netherlands) on the same day of acoustic measurement (Fig. 3a).

A mean radius R_m of 1.93 µm and standard deviation σ of 0.16 µm (coefficient of variation $\sigma/\mu_r = 0.083$) were extracted by fitting a Gaussian distribution, shown by the dashed red line. Shell stiffness, χ, of 0.65 N/m and shell viscosity, κ_s, of 1×10^{-9} kg/s were derived from a bulk acoustic attenuation experiment, as described in [33], and measured at an acoustic pressure of 10 kPa.

Acoustic camera for characterizing subharmonic sensitivity to ambient pressure variations

To measure the pressure sensitivity of single microbubbles, a water tank was constructed that included three transducers and an underwater speaker, shown schematically in Figure 3b.

High-frequency transducers (HF1 and HF2; V324-SU, 182 Olympus Industrial, Essex, UK) were placed perpendicular to each other and orthogonal to the low-frequency transducer (LF; PA275, Precision Acoustics, Dorchester, UK). The foci of the three transducers were aligned using a 0.075 mm needle hydrophone (Precision Acoustics). Figure 3b, inset, shows the transmission pulses. The HF probing signal transmitted by HF1 (25 MHz, 325 μs, 500 kPa) extended before and after the LF signal (starting at t = 0) by 37.5 μs to obtain a reference HF-scattered signal from the non-vibrating bubble. Transmitted LF signals and ambient pressure modulation were the same as described in the numerical methods (LF, 100 kPa, f_T 4.0, 4.5 or 5.5 MHz; speaker, 2.66 kPa [20 mm Hg], 20 kHz around the hydrostatic pressure of 104 kPa). The scattered microbubble signal (Fig. 3c) was then received by HF2, pre-amplified (AU-151910289, Miteq, Hauppauge, NY, USA) and sent to an analog-to-digital converter (PC/ADC; M4x.4420-x4, Spectrum Instrumentation, Limerick, Ireland). To avoid pre-insonifying microbubbles a trigger was implemented, as described by Nawijn et al [34].

The three LF driving signals (f_T of 4.0, 4.5 and 5.5 MHz) were transmitted in separate experiments and measurements were repeated four times per f_T (12 in total). The transmitted speaker pressure was calibrated using a TC4038 hydrophone (Teledyne RESON, Slangerup, Denmark), and the LF and HF pressures were calibrated using a 0.2 mm needle hydrophone (Precision Acoustics) in a separate setup.

Before each measurement, 2 μL microbubble suspension from the collection vial was diluted in 1.8 L (300 microbubbles/mL) phosphate-buffered saline solution and added to the acoustic camera setup, and the suspension was continuously stirred during the 20-min acquisition using a magnetic stirrer. A stylized microbubble signal is shown in Figure 3c, where the microbubble signals were demodulated with respect to the HF probing signal to obtain the radial strain $\varepsilon(t)$ signal as described in [23]. Two measured examples of $\varepsilon(t)$ are shown in Figure 4 (a, b). The fundamental strain amplitude $(\varepsilon)^{-}$ and subharmonic strain response *subH* were isolated from $\varepsilon(t)$ and then fit to the P_{amb}, as described in Appendix B.

Approximately 1200 signals were measured for each f_T, from which approximately 700−800 signals with a steady HF signal (HF amplitude drift ≤50% during measurement) were selected, as described in [35]. Consecutively, four inclusion criteria (IC) were applied:

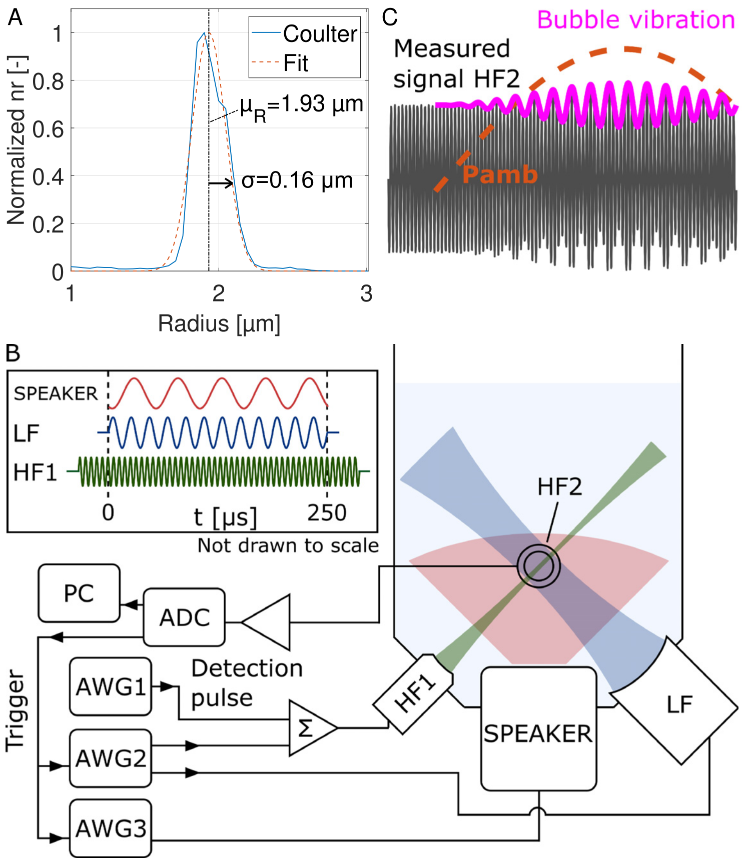

Figure 3. (a) Microbubble size distribution as measured by a Coulter counter, with a Gaussian fit. (b) Acoustic camera setup used for measuring single microbubbles subject to a dynamic ambient pressure induced by the speaker. HF1 transmitted a high-frequency pulse that scattered from a single microbubble and was received by HF2. (c) Bubble vibrations were induced by the low-frequency transducer. A stylized microbubble signal as measured by HF2. ADC, analog-to-digital converter; AWG, arbitrary waveform generator; HF1, high-frequency transducer 1; HF2, high-frequency transducer 2; LF, low frequency.

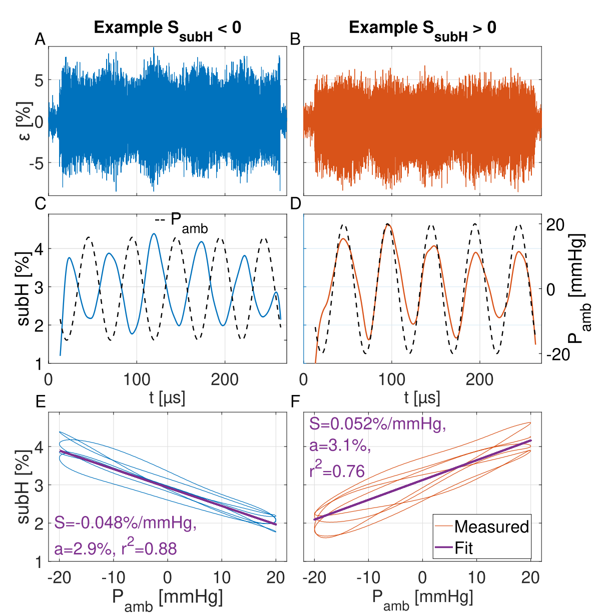

Figure 4. (a, b) Two measured radial strain (ε) signals of individual microbubbles driven at 4.5 MHz. (c, d) The isolated subharmonic strain amplitude *subH*(t) plotted together with the dynamic ambient pressure, and (e, f) the subharmonic strain amplitude plotted as a function of the dynamic ambient pressure *subH* (P_{amb}). Note that for the microbubble in the right column, the subharmonic response increased with ambient pressure, while it decreased for the one in the left column. The corresponding S_{subH} and a_{subH} extracted from a first-order polynomial fit (purple line in e, f).

IC1: Responsive, $\overline{(\varepsilon)} > 0.5\ \%$
IC2: Subharmonic signals, $a_{subH} > 0.5\ \%$
IC3: Sensitive to ambient pressure, $S_{subH} > 0.005\%/\text{mm Hg}$
IC4: Stable sensitive signals, $R^2 > 0.2$

Experimental results

The numbers of microbubbles included for the different f_T are listed in Table 2. The largest percentage of subharmonic microbubbles were encountered at 4.5 MHz (17.3%), followed by 5.5 MHz (13.9%), and the least at 4.0 MHz (2.4%). This occurrence was lower than the 40% observed for SonoVue microbubbles [36], which could be caused by differences in experimental conditions as the microbubbles were unbounded in our study and a single frequency was used. The occurrence was also lower than what could be expected from Figure 2, indicating a larger spread in initial surface tension values, or that differences in shell

Table 2
Number (%) of microbubbles measured for each driving frequency in the first row, and selected after each inclusion criterion (IC1−4).

	f_T [MHz]		
IC	4	4.5	5.5
Signals	718 (100 %)	699 (100 %)	811 (100 %)
Responsive	564 (78.6 %)	553 (79.1 %)	509 (62.8 %)
Subharmonic	17 (2.4 %)	121 (17.3 %)	113 (13.9 %)
Sensitive	16 (2.2 %)	111 (15.9 %)	99 (12.2 %)
Stable	13 (1.8 %)	92 (13.2 %)	86 (10.6 %)

IC, inclusion criteria.

elasticity [29] and smooth-to-buckled transition [31] also played a role. The fraction of stable sensitive signals (IC4) out of the subharmonic signals (IC2) was not dependent on driving frequency (76.1%−76.5%). The fundamental vibrational amplitude of these stable sensitive signals (IC4) was relatively low, *i.e.*, 4.2 ± 1.7, 3.0 ± 0.8 and 2.6 ± 0.6%. Thus, even though a high acoustic driving pressure was used, the destructive effects were minimal as the microbubbles were driven off-resonance. The stable sensitive signals were grouped by the sign of the S_{subH} sensitivity (negative or positive with an increase in P_{amb}), with their averaged responses shown in Figure 5. The left column displays *subH* as a function of time for negative sensitivity, the middle column that for positive sensitivity, while the right column shows *subH* as a function of P_{amb} for both groups. Standard deviations are indicated by the shaded regions. Figure 5a shows that no negative S_{subH} responses were encountered (n = 0), while Figure 5b shows that 12 positive S_{subH} responses were encountered at a driving frequency f_{T} of 4.0 MHz. Positive S_{subH} responses were two times more likely at 4.5 MHz (61 vs. 32) but negative S_{subH} were three times more likely at 5.5 MHz (63 vs. 19). The negative S_{subH} responses in Figure 5 (d, g) had a lower S_{subH}, *i.e.*, a weaker slope of *subH* with P_{amb}, but a higher a_{subH} compared with the positive S_{subH} responses. Interestingly, a stronger sensitivity to ambient pressure for the positive response was also observed in earlier studies on polydisperse microbubbles [20,37].

The *subH*(*t*) decreased over time for the positive S_{subH} responses, as seen in Figure 5 (b, e, h), but remained stable for the negative S_{subH} (t) responses, seen in Figure 5 (d, g). The S_{subH} amplitude remained constant over time for negative and positive sensitivity.

Comparing *subH* as a function of the P_{amb} cyclic variations in Figure 5 (f, i) shows that the positive-sensitivity (orange) signals formed loops as a function of ambient pressure, whereas the negative (blue) signals linearly increased/decreased as a function of ambient pressure (not showing such hysteresis). This indicates that the positive signals exhibited a lag (or phase shift) between the applied pressure and the resulting *subH* response, which was not seen for the negative signals. In combination with decreasing positive sensitivity over time (Fig. 5b, 5e, 5h), this could indicate that the positive-sensitivity signals experienced a higher degree of irreversible changes compared with the negative-sensitivity signals. This is reflected in a better regression R^2 with pressure for negative S_{subH}.

The S_{subH} and *subH* for individual microbubble responses are displayed as a 2-D histogram in Figure 6. Figure 6 (d−f) clearly shows the shift from positive to negative S_{subH} for increasing f_T, as expected. At 4.0 MHz (Fig. 6a), all responses had an a_{subH} below 4% with a relatively strong S_{subH}. At 4.5 MHz (Fig. 6b), relatively strong a_{subH} were measured both with negative and positive S_{subH}, but negative S_{subH} were more likely to have a strong *subH*. At 5.5 MHz (Fig. 6c) the behavior was mostly similar, with the majority being negative S_{subH} responses with comparable a_{subH} and S_{subH} values.

Finally, we noticed that the improved regression of *subH* with P_{amb} for negative responses in Figure 5 was confirmed in simulations in Figure 2 (c, f, g). This is noteworthy, considering that the destructive effects were not simulated. It should also be noted that a linear relationship between *subH* and P_{amb} is not essential for the intended purpose of non-invasive blood pressure sensing, but a monotonic and stable microbubble response is required. Realizing that the effective elasticity χ_{eff}, and with that $f_{0,eff}$, drives subharmonic sensitivity can help imaging strategies for subharmonic blood pressure estimation. Although the results here do not directly allow a comparison between the range of

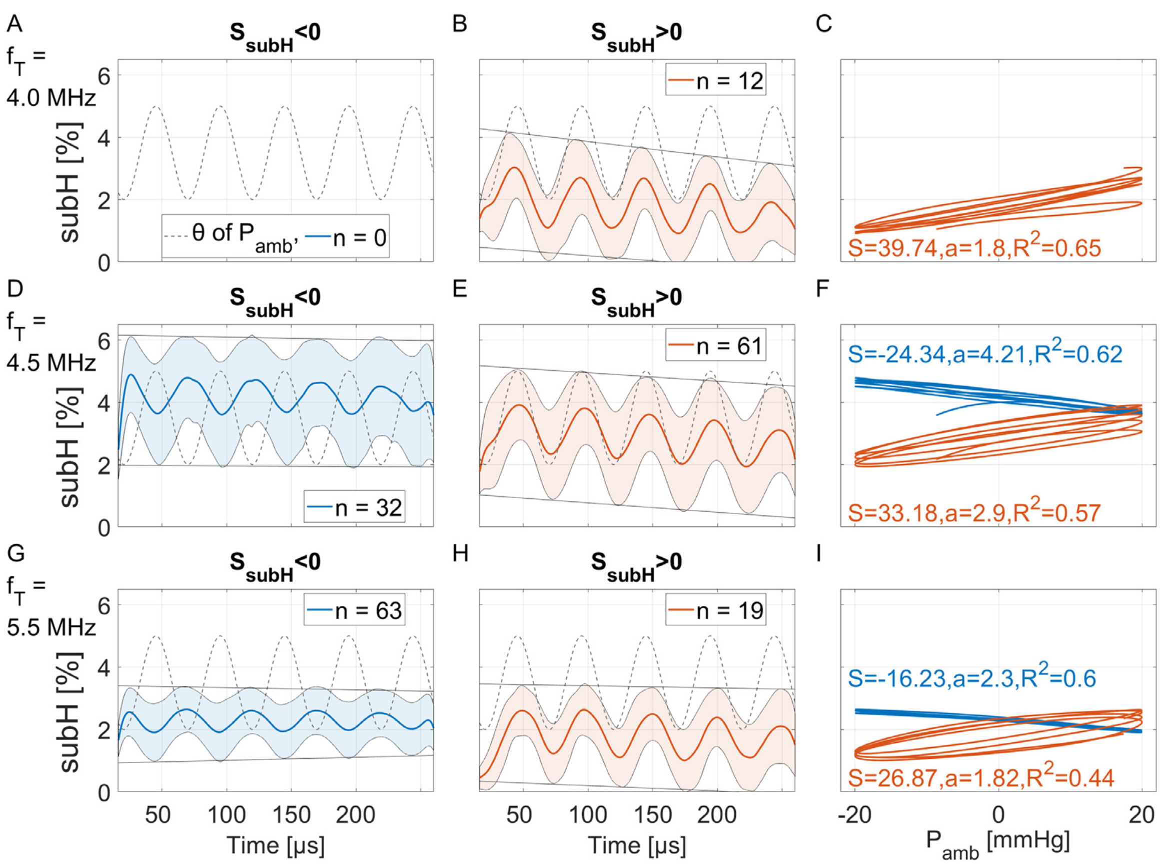

Figure 5. (a, d, g) Averaged *subH* responses grouped for all negative-sensitivity S_{subH} (*left column*) and grouped for (b, e, h) all positive S_{subH} (*middle column*) microbubble responses in response to (a−c) 4.0 MHz, (d−f) 4.5 MHz and (g−i) 5.5 MHz. Shaded regions indicate standard deviations. (a) Is empty as no positive (n = 0) negative sensitive signals were obtained at 4.0 MHz. (c, f, i) *subH* plotted as a function of applied ambient pressure (*right column*).

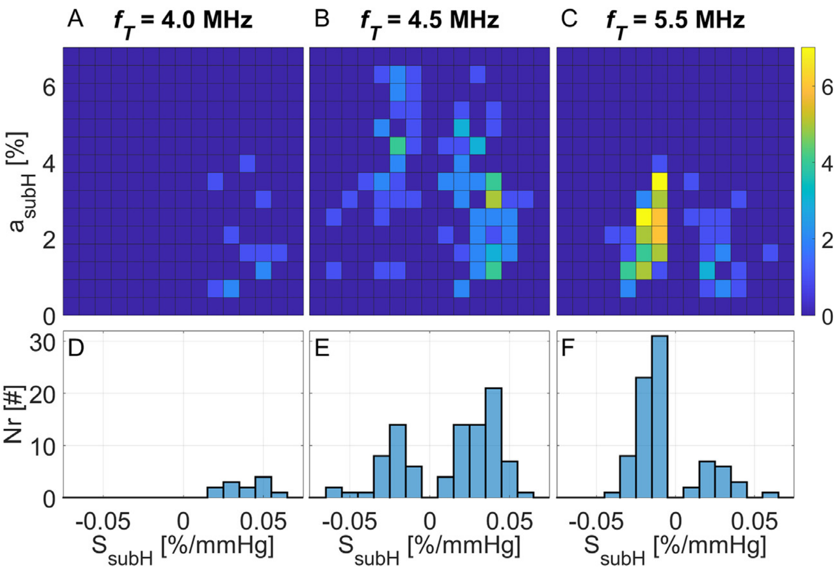

Figure 6. 2-D histograms of subharmonic amplitude a_{subH} and subharmonic pressure sensitivity S_{subH} obtained from measurements with a (a) 4.0 MHz, (b) 4.5 MHz and (c) 5.5 MHz excitation frequency. (d−f) Corresponding histograms of S_{subH}.

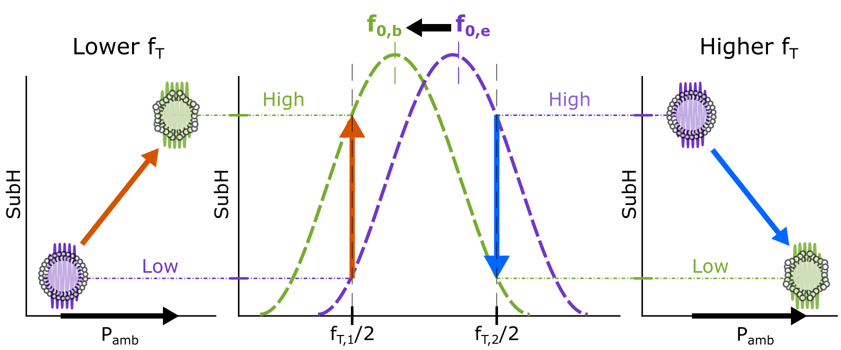

Figure 7. Ambient pressure sensing via subharmonics. The driving frequency, f_T, is close to twice the bubble resonance frequency, f_0. In response to an increased ambient pressure P_{amb} (*black arrows*), the bubble compresses and the lipid shell moves closer to a buckled state, resulting in a resonance frequency that decreases from the elastic $f_{0,e}$ to the buckled $f_{0,b}$. This results in an increased subharmonic amplitude *subH* (*orange arrow/left graph*) if the resonance f_0 moves toward $f_T/2$ and in a decreased *subH* (*blue arrow/right graph*) if f_0 moves away from $f_T/2$.

available contrast agents, insight into the mechanism can help to understand, predict and optimize the sensitivity of microbubble responses to ambient pressure. In future work it would be interesting to simulate the subharmonic ensemble response for varying microbubble size distribution and shell parameters to understand the benefits of monodisperse microbubbles for non-invasive pressure sensing.

Ambient pressure sensitivity of low oscillation-amplitude subharmonics

In summary, the mechanism that drives the ambient pressure sensitivity of subharmonic oscillations is summarized in Figure 7. This mechanism comprises non-linear shell stiffness that decreases when a higher ambient pressure is experienced as the microbubble compresses and the lipid shell is pushed further into the tensionless buckled regime. As a result, the effective surface elasticity decreases and the resonance frequency changes, in turn affecting the subharmonic response. The subharmonic oscillation amplitude was at its maximum when the effective resonance frequency coincided with half the driving frequency, *i.e.*, at the subharmonic frequency. Positive sensitivity (orange arrow in Fig. 7) occurred when the resonance frequency moved toward the subharmonic frequency and negative sensitivity (blue arrow in Fig. 7) occurred when the effective resonance frequency moved away from the subharmonic frequency. Note that this mechanism also holds for free gas bubbles driven at a higher acoustic amplitude, where a similar subharmonic pressure-sensitivity relationship was earlier found by Katiyar et al. [13], which is further discussed in Appendix C.

Conclusion

This study explains the ambient pressure sensitivity of subharmonic vibrations in lipid-coated microbubbles. The subharmonic sensitivity to ambient pressure can be understood by a decrease in resonance frequency when an ambient pressure increase brings the shell closer to a buckled state. Depending on the choice of the driving frequency f_T, the subharmonic amplitude increases when the ambient pressure moves the bubble more into resonance at half the driving frequency $f_T/2$, and the subharmonic amplitude decreases when the resonance shifts further away from $f_T/2$.

To numerically and experimentally investigate this mechanism, the ambient pressure sensitivity was simulated and measured on single microbubbles while vibrating in response to low acoustic amplitude at different driving frequencies, f_T. An f_T of 4.0 MHz exclusively resulted in increasing subharmonics with ambient pressure, while a higher f_T increasingly shifted the bias toward decreasing subharmonics with ambient pressure, as expected. We confirmed (in Appendix C) that this also holds for the high acoustic amplitude subharmonics of free gas bubbles, where a similar relationship was identified by Katiyar et al. [13].

The results show that both positive sensitivity to ambient pressure ($f_T < 2{\cdot}f_{0,eff}$) as well as negative sensitivity ($f_T > 2{\cdot}f_0,eff$) can be utilized to estimate the ambient pressure, as microbubble vibrations are non-destructive regardless of direction. The subharmonic responses that increased with ambient pressure showed a stronger response to ambient pressure changes but a weaker response to subharmonic amplitude. The highest driving frequency f_T of 5.5 MHz resulted in the most robust ambient pressure sensitivity and therefore the most predictable output.

Conflict of interest

The authors have no conflicts to disclose.

Acknowledgments

The work described in this article was funded by project Bubble-X of the research program Ultra-X-Treme (P17-32), financed by the Dutch Research Council (NWO). The authors thank Michiel Manten from the Department of Experimental Medical Instrumentation and Robert Beurskens from the Department of Biomedical Engineering, both from Erasmus MC University Medical Center Rotterdam, The Netherlands, for technical assistance.

Data availability statement

The data that support the findings of this study are available from the corresponding author upon reasonable request.

Supplementary materials

Supplementary material associated with this article can be found in the online version at doi:10.1016/j.ultrasmedbio.2025.01.016.

Appendix A. Numerical signal processing

The simulated microbubble responses were normalized to the initial radius following $\varepsilon = (R - R_0)/R_0$ [23]. From this strain ε response, the subharmonic strain component $\varepsilon_{f/2}(t)$ was isolated by a second-order zero-phase band pass filter, centered at half the excitation frequency (f_T/2; 100 kHz bandwidth). From $\varepsilon_{f/2}(t)$, the subharmonic strain component *subH* (t) was isolated using the analytic modulus and a 1.2 µs time smoothing window. Thus, in short:

$$\varepsilon(t) \overset{\text{filter}}{\rightarrow} \varepsilon_{f/2}(t) \overset{\text{envelope}}{\rightarrow} subH(t), subH(P_{amb}).$$

Appendix B. Experimental signal processing

A stylized microbubble signal is shown in Figure 3c and an example measured signal is shown in Figure B.8. The measured microbubble signals (A and B) were demodulated with respect to the HF probing signal by calculating the analytic modulus. From this analytic modulus, the mean level was determined using the signal before and after the LF signal was transmitted (marked ref in A) as a measure for the reference-scattered HF intensity. This reference HF intensity was then subtracted from the analytic modulus and the result divided by the mean HF level, as described in [23], to obtain the radial strain signal $\varepsilon(t)$, as shown in (C and D). Two measured examples of $\varepsilon(t)$ are shown in Figure 4 (a, b). The fundamental strain amplitude $(\bar{\varepsilon})$ was extracted from the frequency domain. The subharmonic strain component $\varepsilon_{f/2}(t)$ and the subharmonic strain component *subH*(t), as shown in (E), were isolated in the same way as the numerical responses.

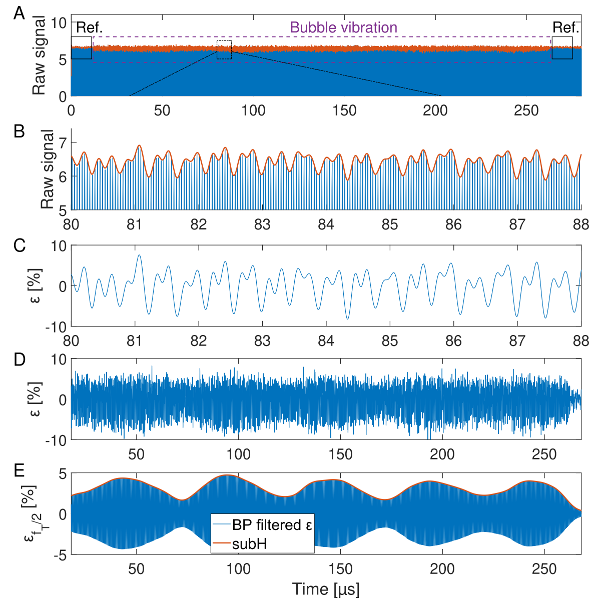

Figure B.8 (a)Measured HF signal with sections used for reference indicated with black squares and the amplitude-modulated bubble vibration shown in orange and indicated by purple square. (b) Magnification of HF signal from 80 to 88 μs. (c) Demodulated strain ε signal from 80 to 88 µs. (d) Demodulated strain e signal over the full duration. (e) ε signal bandpass filtered around the subharmonic frequency f = 2.25 MHz in blue, and *subH* obtained from the envelope of the BP-filtered ε signal shown in orange.

The subharmonic response, *subH*, plotted as a function of time (Fig. 4c, 4d), was plotted together with the dynamic ambient pressure and as a function of said P_{amb} (Fig. 4e, 4f), which shows a looping pattern because of the four P_{amb} cycles. The response of $subH(P_{amb})$ was seen to decrease or increase as a function of P_{amb}. The $subH(P_{amb})$ of each measured microbubble signal was fitted with respect to P_{amb} using eqn (5), also displayed by the straight purple lines in Figure 4 (e, f). To capture the steady state subharmonic behavior, the number of ambient pressure cycles used to fit eqn (5) correspond to four cycles starting from the first positive peak.

Appendix C. Ambient pressure sensitivity of higher oscillation-amplitude subharmonics

Subharmonic microbubble oscillations have also been encountered at acoustic amplitudes higher than those investigated here. These subharmonic oscillations are not related to the shell buckling mechanism but to intrinsic non-linearities in the dynamics of the gas core. Of particular interest is the onset of subharmonics in the ‘growth regime’ [5,38] before the inertial cavitation regime [12], as the subharmonics here show robust sensitivity to ambient pressure [5,7,39].

When subjected to high acoustic pressures, the contribution of the shell becomes negligible [17] and the dynamics approach that of an uncoated gas bubble. The relationship between subharmonics ambient pressure sensitivity and the initial microbubble resonance frequency for free gas bubbles has been investigated numerically before by Katiyar et al. [13]. They associated the initial microbubble resonance with the change in subharmonic amplitude under the influence of static pressure and found a positive subharmonic sensitivity for initial resonance frequencies between 1.4 and 1.6 times the driving frequency as well as negative sensitivity when the initial resonance frequency exceeded 2.1 times the driving frequency. The resonance frequency $f_{0,eff}$ of a free gas bubble depends on the ambient pressure explicitly (see eqn [4]) and implicitly by its effective radius [40], and thus increases with a static pressure increase as it compresses the gas core. Additionally, the resonance frequency of free gas bubbles decrease with the amplitude of oscillation as the rarefaction phase becomes increasingly favored over the compression phase [11,30,40].

Here we studied the relationship between the ambient pressure sensitivity of the higher acoustic amplitude subharmonics of un-coated microbubbles with its effective resonance frequency. As the radius at high acoustic amplitudes easily spans a factor of 10, which cannot be experimentally measured with an acoustic camera, we investigated these dynamics numerically.

Appendix C.1. Methods

The response of an un-coated microbubble to a 4 MHz acoustic pulse with a duration of 25 μs (75 cycles) was simulated by solving eqn (1) with $\kappa_s = 0$ and $\sigma(R) = \sigma_w$. The static pressure was set to linearly increase in time from 101.3 to 111.3 kPa over the 25 μs duration of the microbubble oscillation. The other parameters were set to the values listed in Table 1. This simulation was performed for microbubble radii of 0.75−4 μm over 100 steps, and for acoustic amplitudes from 100 to 500 kPa over 80 steps.

From the simulated radius-time curves, the strain was derived and filtered around the subharmonic frequency of 2 MHz using a 300 kHz bandwidth following the same approach as described in Appendix A. The subharmonic strain amplitude *subH* was then fitted to the applied ambient pressure using eqn (5) to obtain a_{subH} and S_{subH}. The effective resonance frequency $f_{0,eff}$ was obtained from the time-averaged radius over the full duration R_{mean} by eqn (C.1):

$$f_{0,eff} = \frac{1}{2\pi R_{mean}}\sqrt{\frac{1}{\rho}\left(3\kappa P_{amb} + (3\kappa - 1)\frac{2\sigma_w}{R_{mean}}\right)}. \tag{C.1}$$

To identify the inertial cavitation regime, we followed the common definition of $R_{max} = 2R_0$ [41].

Appendix C.2. Results

The subharmonic sensitivity S_{subH} and mean subharmonic amplitude a_{subH} of the simulated free gas bubble responses are shown in Figure C.9 from radii ranging 0.75−3 μm. The subharmonic regime shown in Figure C.9b started at an acoustic amplitude of 150 kPa for microbubbles with an R_0 of 1.8 μm. When the acoustic amplitude increased, the range of bubble radii that showed subharmonics increased. The microbubbles with radii above 2.5 μm showed no subharmonics. The microbubble size that corresponded with the strongest subharmonic amplitude is well approximated by the dashed black line that denotes when the effective resonance frequency $f_{0,eff}$ equals $f_T/2$. This $f_{0,eff}$ showed a decreasing size for increasing pressure amplitude due to the favored rarefaction of the oscillation [30].

The sensitivity shown in Figure C.9a shows both negative and positive sensitivity, which were strongest in magnitude at the edges of the subharmonic regime. Negative sensitivity was observed when $f_{0,eff} \geq f_T/2$ and positive sensitivity when $f_{0,eff}$ was below $f_T/2$. The negative sensitivity generally had a higher magnitude, which increased to -0.7%/mm Hg, whereas the strongest positive sensitivity was 0.5%/mm Hg. Furthermore, the range of microbubble sizes exhibiting negative sensitivity for a given driving frequency was much larger, above 300 kPa. This qualitatively matches with the observed trend that at higher acoustic amplitudes, negative subharmonic sensitivity to ambient pressure is observed regardless of the type of contrast agent used [5,7]. Note that the relationship between the subharmonic sensitivity and the effective resonance frequency here was mirrored compared with the sensitivity for low amplitude-driven shelled microbubbles, as shown in Figure 2. This is because additional static pressure generally increases the resonance frequency of free gas bubbles as the gas core is compressed [13], while additional static pressure generally decreases the resonance frequency of shelled microbubbles as the lipid shell becomes increasingly buckled.

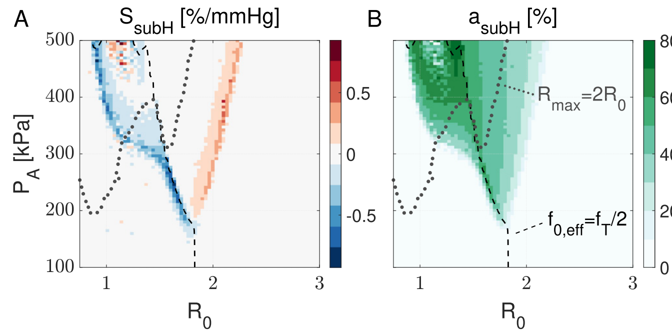

Figure C.9 Simulated subharmonic sensitivity to (a) ambient pressure S_{subH} and (b) baseline subharmonic strain magnitude a_{subH} of a free gas bubble as a function of resting radius R_0 and acoustic amplitude Pa. The inertial cavitation regime $R_{max} = 2R_0$ is indicated by the gray dotted line and the dashed black line marks when the effective resonance frequency $f_{0,eff}$ equals half the driving frequency.

The inertial cavitation threshold $R_{max} = 2R_0$ is shown by the dotted gray line in Figure C.9, which shows that at 200 kPa, microbubbles with a 0.9 μm radius exceeded the inertial cavitation threshold, and that this threshold was exceeded for larger microbubbles at higher acoustic pressures. In that case, the smaller microbubbles generated much stronger subharmonic scattering than larger microbubbles, which further skewed subharmonic sensitivity to ambient pressure toward negative sensitivity [11,30]. However, this assumed that the lipid shell was already destroyed. If this sensitivity behavior was simulated for microbubbles with a coating, the acoustic amplitude threshold for subharmonic generation increased considerably (a factor of two or more) due to an additional damping effect of the shell and the buckling mechanism [40]. These simulations are therefore not meant as a direct comparison with previous subharmonic sensitivity results, but to highlight that the effective resonance frequency approach can also predict subharmonic sensitivity at higher acoustic amplitudes.

Appendix C.3. Conclusion

The subharmonic sensitivity of free gas bubbles driven at high acoustic amplitudes was investigated numerically. Subharmonic exhibited maximum readings when the driving frequency was set to twice the effective resonance frequency. The effective resonance frequency of a free gas bubble increased as the size decreased under a static pressure increase, but decreased with increasing oscillation amplitude. Negative sensitivity corresponded with stronger microbubble oscillations and higher sensitivity magnitudes, which could explain why mostly negative sensitivity was observed at high acoustic amplitude-driven subharmonics.

References

[1] Tickner EG. Precision microbubbles for right side intracardiac pressure and flow measurements editor. In: Rijsterborgh H, editor. Echocardiology. Dordrecht: Springer Netherlands; 1981. p. 461–72.

[2] Bouakaz A, Frinking PJ, de Jong N, Bom N. Noninvasive measurement of the hydrostatic pressure in a fluid-filled cavity based on the disappearance time of micrometer-sized free gas bubbles. Ultrasound Med Biol 1999;25:1407–15.

[3] Shi WT, Forsberg F, Raichlen JS, Needleman L, Goldberg BB. Pressure dependence of subharmonic signals from contrast microbubbles. Ultrasound Med Biol 1999;25:275–83.

[4] Liu S, Wu J, Gu Y, Guo X, Tu J, Xu D, et al. Ambient pressure evaluation through subharmonic response of chirp-sonicated microbubbles. Ultrasound Med Biol 2017;43:332–40.

[5] Halldorsdottir VG, Dave JK, Leodore LM, Eisenbrey JR, Park S, Hall AL, et al. Subharmonic contrast microbubble signals for noninvasive pressure estimation under static and dynamic flow conditions. Ultrason Imaging 2011;33:153–64.
[6] Wang Y, Lu H, Huang L, Li D, Qiu W, Li L, et al. Noninvasive estimation of tumor interstitial fluid pressure from subharmonic scattering of ultrasound contrast microbubbles. Biosensors 2023;13:528.
[7] Azami RH, Forsberg F, Eisenbrey JR, Sarkar K. Ambient pressure sensitivity of the subharmonic response of coated microbubbles: Effects of acoustic excitation parameters. Ultrasound Med Biol 2023;49:1550–60.
[8] Nio AQX, Faraci A, Christensen-Jeffries K, Raymond JL, Monaghan MJ, Fuster D, et al. Optimal control of SonoVue microbubbles to estimate hydrostatic pressure. IEEE Trans Ultrason Ferroelectr Freq Control 2020;67:557–67.
[9] Prosperetti A. A general derivation of the subharmonic threshold for non-linear bubble oscillations. J Acoust Soc Am 2013;133:3719–26.
[10] Song JH, Moldovan A, Prentice P. Nonlinear acoustic emissions from therapeutically driven contrast agent microbubbles. Ultrasound Med Biol 2019;45:2188–204.
[11] Gümmer J, Schenke S, Denner F. Modelling lipid-coated microbubbles in focused ultrasound applications at subresonance frequencies. Ultrasound Med Biol 2021;47:2958–79.
[12] Bader KB, Holland CK. Gauging the likelihood of stable cavitation from ultrasound contrast agents. Phys Med Biol 2013;58:127–44.
[13] Katiyar A, Sarkar K, Forsberg F. Modeling subharmonic response from contrast microbubbles as a function of ambient static pressure. J Acoust Soc Am 2011;129:2325–35.
[14] Hoff L, Sontum PC, Hovem JM. Oscillations of polymeric microbubbles: Effect of the encapsulating shell. J Acoust Soc Am 2000;107:2272–80.
[15] Faez T, Renaud G, Defontaine M, Calle S, de Jong N. Dynamic manipulation of the subharmonic scattering of phospholipid-coated microbubbles. Phys Med Biol 2011;56:6459–73.
[16] Sijl J, Dollet B, Overvelde M, Garbin V, Rozendal T, de Jong N, et al. Subharmonic behavior of phospholipid-coated ultrasound contrast agent microbubbles. J Acoust Soc Am 2010;128:3239–52.
[17] Marmottant P, van der Meer S, Emmer M, Versluis M, de Jong N, Hilgenfeldt S, et al. A model for large amplitude oscillations of coated bubbles accounting for buckling and rupture. J Acoust Soc Am 2005;118:3499–505.
[18] Tremblay-Darveau C, Williams R, Burns PN. Measuring absolute blood pressure using microbubbles. Ultrasound Med Biol 2014;40:775–87.
[19] Andersen KS, Jensen JA. Impact of acoustic pressure on ambient pressure estimation using ultrasound contrast agent. Ultrasonics 2010;50:294–9.
[20] Prinking PA, Gaud E, Brochot J, Arditi M. Subharmonic scattering of phospholipid-shell microbubbles at low acoustic pressure amplitudes. IEEE Trans Ultrason Ferroelectr Freq Control 2010;57:1762–71.
[21] Nio AQX, Faraci A, Christensen-Jeffries K, Eckersley RJ, Monaghan MJ, Raymond JL, et al. The subharmonic amplitude of SonoVue increases with hydrostatic pressure at low incident acoustic pressures. Paper presented at: 2017 IEEE International Ultrasonics Symposium (IUS); 2017. p. 1–4.
[22] Li F, Cai F, Meng L, Jin Q, Zhen H, Li D. Enhanced ambient pressure sensitivity of the subharmonic signal from ultrasound contrast microbubbles. Paper presented at: IEEE International Ultrasonics Symposium; 2013. p. 325–8.
[23] Renaud G, Bosch JG, van der Steen AFW, de Jong N. An acoustical camera for in vitro characterization of contrast agent microbubble vibrations. Appl Phys Lett 2012;100:101911.
[24] Overvelde M, Garbin V, Sijl J, Dollet B, de Jong N, Lohse D, et al. Nonlinear shell behavior of phospholipid-coated microbubbles. Ultrasound Med Biol 2010;36:2080–92.
[25] Kumar KN, Sarkar K. Effects of ambient hydrostatic pressure on the material properties of the encapsulation of an ultrasound contrast microbubble. J Acoust Soc Am 2015;138:624–34.
[26] Kumar KN, Sarkar K. Interfacial rheological properties of contrast microbubble Targestar P as a function of ambient pressure. Ultrasound Med Biol 2016;42:1010–7.
[27] van der Meer SM, Dollet B, Voormolen MM, Chin CT, Bouakaz A, de Jong N, et al. Microbubble spectroscopy of ultrasound contrast agents. J Acoust Soc Am 2007;121:648–56.
[28] Averkiou MA, Bruce MF, Powers JE, Sheeran PS, Burns PN. Imaging methods for ultrasound contrast agents. Ultrasound Med Biol 2020;46:498–517.
[29] Spiekhout S, van Elburg B, Voorneveld J, de Jong N, Versluis M, Bosch JG, et al. Are monodisperse phospholipid-coated microbubbles mono-acoustic? Appl Phys Lett 2024;124:231601.
[30] Leighton TG. The acoustic bubble. London: Academic Press; 1994 ISBN 0-12-441920-8.
[31] Sijl J, Overvelde M, Dollet B, Garbin V, de Jong N, Lohse D, et al. Compression-only behavior: A second-order nonlinear response of ultrasound contrast agent microbubbles. J Acoust Soc Am 2011;129:1729–39.
[32] Abou-Saleh RH, Armistead FJ, Batchelor DV, Johnson BR, Peyman SA, Evans SD. Horizon: Microfluidic platform for the production of therapeutic microbubbles and nanobubbles. Rev Sci Instrum 2021:92074105.
[33] Segers T, Gaud E, Versluis M, Frinking P. High-precision acoustic measurements of the nonlinear dilatational elasticity of phospholipid-coated monodisperse microbubbles. Soft Matter 2018;14:9550–61.
[34] Nawijn CL, Spiekhout S, Voorneveld S, Bosch JG, Versluis M, Segers T, Lajoinie GPR. Stress-strain analysis of single ultrasound-driven microbubbles for viscoelastic shell characterization. J Acoust Soc Am 2025;157(2):897–911.
[35] Spiekhout S, Voorneveld J, van Elburg B, Renaud G, Segers T, Lajoinie GPR, et al. Time-resolved absolute radius estimation of vibrating contrast microbubbles using an acoustical camera. J Acoust Soc Am 2022;151:3993–4003.
[36] Faez T, Emmer M, Docter M, Sijl J, Versluis M, de Jong N. Characterizing the subharmonic response of phospholipid-coated microbubbles for carotid imaging. Ultrasound Med Biol 2011;37:958–70.
[37] Sun T, Jia N, Zhang D, Xu D. Ambient pressure dependence of the ultra-harmonic response from contrast microbubbles. J Acoust Soc Am 2012;131:4358–64.
[38] Halldorsdottir V, Dave J, Eisenbrey J, Machado P, Zhao H, Liu J, et al. Subharmonic aided pressure estimation for monitoring interstitial fluid pressure in tumours in vitro and in vivo proof of concept. Ultrasonics 2014;54:1938–44.
[39] Azami RH, Forsberg F, Eisenbrey JR, Sarkar K. Acoustic response and ambient pressure sensitivity characterization of SonoVue for noninvasive pressure estimation. J Acoust Soc Am 2024;155:2636–45.
[40] Qin D, Lei S, Wang X, Zhong X, Ji X, Li Z. Resonance behaviors of encapsulated microbubbles oscillating nonlinearly with ultrasonic excitation. Ultrason Sonochem 2023;94:106334.
[41] Wang M, Zhou Y. Numerical investigation of the inertial cavitation threshold by dual-frequency excitation in the fluid and tissue. Ultrason Sonochem 2018;42:327–38.